CrossMark

Rapid sintering of MoS₂ counter electrode using near-infrared pulsed laser for use in highly efficient dye-sensitized solar cells

Hansol Jeong [a, b, 1], Jae-Yup Kim [c, 1], Bonkee Koo [b, d], Hae Jung Son [a, b], Dongwhan Kim [a, e], Min Jae Ko [a, b, f, *]

[a] Green School, Korea University, Seoul, 02841, Republic of Korea
[b] Photo-Electronic Hybrids Research Center, Korea Institute of Science and Technology (KIST), Seoul, 02792, Republic of Korea
[c] Department of Electrical and Computer Engineering, Seoul National University, 1 Gwanak-ro, Gwanak-gu, Seoul, 08826, Republic of Korea
[d] Department of Chemical and Biological Engineering, Korea University, Seoul, 02841, Republic of Korea
[e] Department of Material Science and Engineering, Korea University, Seoul, 02841, Republic of Korea
[f] KU-KIST Graduate School of Converging Science and Technology, Korea University, Seoul, 02841, Republic of Korea

HIGHLIGHTS

- Highly efficient MoS₂ counter electrodes are prepared at a low temperature.
- A near-IR pulsed laser is proposed for post-sintering of MoS₂ films.
- Laser-sintered MoS₂ counter electrodes exhibit a comparable performance with Pt.

GRAPHICAL ABSTRACT
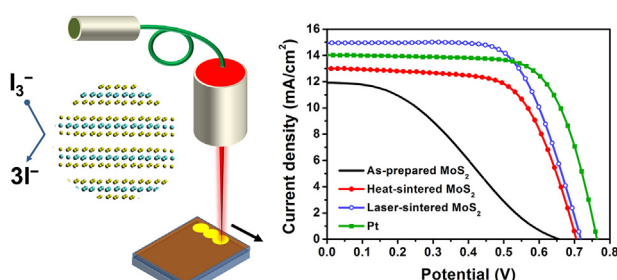
ARTICLE INFO

ABSTRACT

Molybdenum disulfide (MoS₂) is a promising material for use as a low-cost electrocatalytic counter electrode (CE) in photoelectrochemical dye-sensitized solar cells (DSSCs). However, currently, the MoS₂ CEs are generally prepared with a high temperature sintering for the synthesis and crystallization of MoS₂. Here, we report a simple and rapid method for the preparation of highly efficient MoS₂ CEs. The MoS₂ films were synthesized at 70 °C, followed by sintering with a near-infrared (IR) pulsed laser for 1 min. Compared to the conventional heat-sintered MoS₂ CE, the laser-sintered CE showed enhanced crystallinity and improved interconnection between the MoS₂ particles, resulting in superior electrocatalytic activity towards the I^-/I_3^- redox couple. When used in a DSSC, the laser-sintered MoS₂ CE exhibited a higher conversion efficiency ($\eta = 7.19\%$) compared to that of the heat-sintered CE ($\eta = 5.96\%$). Furthermore, the laser-sintered CE had a comparable conversion efficiency compared to that of the conventional Pt CE ($\eta = 7.42\%$).

* Corresponding author. Green School, Korea University, Seoul, 02841, Republic of Korea.
E-mail address: mjko@kist.re.kr (M.J. Ko).
[1] These authors contributed equally to this work.

1. Introduction

Since the discovery of graphene and its success in a variety of applications [1], two-dimensional (2D) transition-metal dichalcogenides (TMDCs) have received considerable attention as

promising materials for applications in electronics and catalysis [2–15]. Of the TMDCs, molybdenum disulfide (MoS$_2$) has been intensively investigated as a potential material for transistors [4,5], chemical sensors [6], batteries [7,8], electrocatalysts for the hydrogen evolution reaction (HER) [9,10], and photovoltaics [11–15]. This broad applicability is possible because of their unique properties including high mobilities, large specific surface areas, and excellent catalytic activities. In particular, it has been reported that MoS$_2$ is a promising electrocatalytic counter-electrode (CE) material for next-generation photovoltaics, such as dye-sensitized solar cells (DSSCs) [12–18]. DSSCs are regarded as potential alternatives to conventional silicon solar cells due to the low cost of materials, their high conversion efficiencies, the simplicity of their fabrication, and potential flexibility [19–25]. To obtain a highly efficient DSSC, the CE should efficiently catalyze the reduction of the redox couple in the electrolyte. Pt is the conventional CE material, and it is currently the electrode with the best electrocatalytic activity toward the iodide/triiodide redox couple (I$^-$/I$_3^-$) used in DSSCs. However, the high cost and rarity of Pt limit its practical use [21,26–29].

Therefore, various Pt-free CEs have been suggested as possible alternatives to the high cost Pt CE. For instance, the CEs based on metal sulfides (FeS$_2$, NiS$_2$, WS$_2$) [12,30,31], carbides (WC, MoC) [32] and nitrides (TiN, NiN) [33,34] exhibited reasonable conversion efficiencies around 7–8%. In addition, alloy CEs including Co-Ni [35], Fe-Se [36], Co-Se [37], Ru-Se [38] showed promising conversion efficiencies above 8%. Furthermore, several CEs based on conducting polymers or carbon materials demonstrated high conversion efficiencies around 9–10% with iodine or cobalt redox couples [39-42]. Among those materials for Pt-free CEs, MoS$_2$ is one of the most promising alternatives to Pt because of its low cost, abundance, chemical stability, and excellent catalytic activity.

Currently, MoS$_2$ CEs are generally prepared *via* chemical reactions that are carried out at 200–800 °C [12,14–18], followed by post-sintering at 300–500 °C to crystallize the MoS$_2$ [12,13,16]. However, the generation of these harsh conditions is expensive, and high temperatures are not compatible with flexible plastic substrates [21,25,43]. If truly low-cost photovoltaics are to be realized, both material and processing costs must be reduced [25,44]. To this end, we have developed a rapid and simple fabrication process for MoS$_2$ electrocatalytic CEs. In our process, MoS$_2$ was synthesized at a relatively low temperature (70 °C), followed by rapid sintering (about 1 min) at room temperature using a near-infrared (IR) pulsed laser. Despite the rapid and simple fabrication process, the laser-sintered MoS$_2$ CE showed a higher conversion efficiency than that of the heat-sintered CE; furthermore, it had a comparable conversion efficiency to that of the conventional Pt CE when used in DSSCs. To reveal the electrocatalytic activity of laser-sintered MoS$_2$ CE and the effect of laser-sintering on the electrode surface morphology, the crystal structure and chemical states of a laser-sintered MoS$_2$ film were investigated. Furthermore, the electrocatalytic activities of the laser-sintered MoS$_2$, heat-sintered MoS$_2$, and Pt CEs toward the I$^-$/I$_3^-$ redox couple were systematically compared.

2. Experimental details

2.1. Fabrication of the MoS$_2$ and Pt CEs

First, fluorine-doped tin oxide glass (FTO; TEC-8, Pilkington) was sonicated while being washed sequentially with deionized (DI) water and ethanol for 20 min. Then, the FTO glass was dried under a stream of N$_2$. Subsequently, the FTO glass was treated with UV/ozone for 20 min at room temperature. To deposit the MoS$_2$ film, the cleaned FTO glass was immersed in an ethanolic solution containing 0.2 M molybdenum(V) chloride (Aldrich, 95%) and 0.2 M thioacetamide (Aldrich, 99.0%) at 70 °C for 7 h [13]. After finishing the reaction, the MoS$_2$/FTO electrode was washed with ethanol and dried under a stream of N$_2$. Then, post-treatment was carried out, either by a conventional heat-sintering method or our laser-sintering method. The heat sintering was carried out at 350 °C for 30 min under a N$_2$ atmosphere. For comparison, the heat sintering was also performed with the same condition in a forming gas (5 vol % H$_2$ in N$_2$). In contrast, the laser sintering was performed in air using a pulsed ytterbium-doped fiber laser system (ML20-PL-R-OEM, General Microtechnology & Photonics) with a near-infrared IR wavelength (1080 nm). The distance between MoS$_2$/FTO electrode and the laser source was about 22 cm. The pulse duration, pulse repetition rate, and the maximum average power output were 40 ns, 50 kHz, and 20 W, respectively. We controlled the average output power to be from 6 to 10% of the maximum value. The focused laser beam used for sintering had a diameter of 30 μm and a scanning speed of 50 cm/s. Approximately 1 min was required to scan a sample with dimensions of 1 × 1.5 cm. For comparison, a conventional Pt CE was also prepared by a thermal decomposition method. A drop of 7 mM H$_2$PtCl$_6$ solution in iso-propanol was spread onto FTO glass, followed by annealing at 400 °C for 20 min in air.

2.2. Electrode assembly

For the TiO$_2$ working electrode, two kinds of TiO$_2$ pastes were prepared, as described previously [45]. Briefly, a transparent paste of hydrothermally synthesized nanocrystalline TiO$_2$ (20 nm diameter) was prepared. In addition, a scattering paste of TiO$_2$ particles with diameters of 500 nm (G2, Showa Denko, Japan) was prepared. Before the deposition of the TiO$_2$ pastes, the FTO glass was coated with a dense TiO$_2$ blocking layer by spin-casting of a 7.5 wt % Ti(IV) bis(ethylacetoacetato)-diisopropoxide solution in 1-butanol, followed by annealing at 500 °C for 10 min in air. Onto this substrate, the transparent paste was deposited by the doctor blade method, followed by annealing at 150 °C for 10 min in air. Subsequently, the scattering paste was deposited onto the layer of transparent paste by the same method, followed by annealing at 500 °C for 30 min in air. The annealed TiO$_2$ electrode was immersed into a 0.5 mM N-719 dye (Everlight) solution in ethanol for 12 h at room temperature. Then, the dye-adsorbed TiO$_2$ electrode was assembled with the CEs using hot, melted Surlyn 1702 (Dupont, 60 μm-thick). Then, a drop of the electrolyte was injected into the assembled cells through pre-drilled holes onto the CEs. The electrolyte was an acetonitrile solution containing 0.7 M 1-propyl-3-methylimidazoliumiodide (PMII, synthesized), 0.03 M I$_2$ (Aldrich, 99.8%), 0.05 M guanidinium thiocyanate (Aldrich, 97%), and 0.5 M 4-*tert*butylpyridine (Aldrich, 96%). The active area of the assembled cells was approximately 0.40–0.45 cm^2, measured by an image analysis program from data collected with a CCD camera (Moticam 1000).

2.3. Characterization

The morphologies of the MoS$_2$ films were characterized by field-emission scanning electron microscopy (FE-SEM; Hitachi S4100). The surface electronic states of the synthesized MoS$_2$ films were investigated by X-ray photoelectron spectroscopy (XPS; Thermo Fisher Scientific Sigma Probe) using an Al Kα X-ray source. Depth profiling was carried out using a 2 keV Ar$^+$ beam with an etching rate of 18 nm/min. The crystal structures of the films were confirmed using X-ray diffraction (XRD; Rigaku D/MAX 2500 V) with Cu Kα radiation. Cyclic voltammetry (CV) for each CE was carried out using a CHI440 potentiostat-galvanostat (CH Instruments Inc.) at a scan rate of 50 mV/s in an electrolyte containing

10 mM Li, 1 mM I$_2$, and 0.1 M LiClO$_4$ in acetonitrile. Pt wire and a Ag/Ag$^+$ couple were employed as the counter and reference electrodes, respectively. Standard photocurrent density-voltage (*J-V*) measurements were performed using a 1600 W xenon lamp (Yamashita Denso YSS-200A solar simulator with an AM 1.5 G filter) at a power of 100 mW/cm^2. Before the *J-V* measurements, each device was covered by a black aperture mask to avoid overestimation caused by additional illumination from the lateral space [46,47]. The incident light intensity was adjusted using a Si reference solar cell produced by NREL. Incident photon-to-current conversion efficiency (IPCE) spectra were collected under short-circuit conditions with a spectral resolution of 10 nm using a xenon lamp source and a grating monochromator. Symmetric dummy cells of each CE were assembled to obtain the Tafel polarization curves and impedance spectra. These dummy cells were prepared by assembling two identical CEs with hot, melted Surlyn 1702, followed by injection of the iodine electrolyte. The active area at each side of these dummy cells was approximately 0.95 cm^2. The Tafel polarization curves and impedance spectra were obtained for each symmetric dummy cell using a Solartron 1287 potentiostat equipped with a Solartron 1260 frequency-response detector.

3. Results and discussion

Before characterization of the prepared MoS$_2$ films, we optimized the laser-sintering conditions used to prepare the highly efficient MoS$_2$ CEs for DSSCs. Fig. S1 (Supplementary Material) shows the *J-V* characteristics of the DSSCs with MoS$_2$ CEs before and after the laser-sintering process depending on the power output of the laser. The photovoltaic performance parameters for each condition are summarized in Table S1 (Supplementary Material). Compared to the as-prepared film, the laser-sintered films showed greatly enhanced conversion efficiency (η), mainly due to the increased fill factor (*FF*). This increase in conversion efficiency indicates that the electrocatalytic activity of the prepared MoS$_2$ films toward the I$^-$/I$_3^-$ redox couple was enhanced after the laser-sintering process. This enhancement is attributed to the crystallization and increased interconnection between the MoS$_2$ particles, as will be discussed later. The conversion efficiency was optimal at

8% of the maximum output power of the laser (η = 7.19%). This conversion efficiency is 2.62 times greater than that of the as-prepared film (η = 2.74%). However, when the output power was greater than 8% of the maximum laser power, the conversion efficiency decreased compared to that of the optimized value, possibly due to damage to the FTO layer.

We compared the electrocatalytic activity of the laser-sintered MoS$_2$ film (prepared with the optimized laser power, *i.e.*, 8% of the maximum power) with that prepared by conventional heat-sintering and the conventional Pt CE. Fig. 1a compares the surface SEM images of the prepared MoS$_2$ film before and after the sintering process. As shown in the figure, the as-prepared film is composed of spherical grains with random sizes of approximately 250 nm. After the conventional heat-sintering, the spherical shape of the grains was maintained but the grain size increased due to Ostwald ripening [48], increasing to approximately 350 nm. In contrast, after the laser-sintering, the surface morphology changed remarkably. The large grains at the surface likely melted on exposure to the incident laser beam, resulting in a more tightly connected grain structure that is advantageous for efficient electrical conduction. Fig. 1b shows the cross-sectional images of the MoS$_2$ film before and after sintering. After sintering, the film surfaces became flatter. The thicknesses of both heat-sintered and laser-sintered films were approximately 670 nm.

Fig. 2 shows the XRD patterns for the prepared MoS$_2$ films before and after sintering. The diffraction pattern of the as-prepared MoS$_2$ film indicates the presence of an amorphous-like phase; however, one crystalline peak, which corresponds to the (103) plane (JCPDS 37-1492) of the hexagonal MoS$_2$ phase, is observed. The XRD pattern of the heat-sintered film also indicates the presence of an amorphous-like phase in the film. In addition, a reflection, indexed to the (011) peak of the MoO$_3$ phase (JCPDS 37-1445), was observed, indicating partial oxidation of the film. Compared to the heat-sintered film, the laser-sintered film was more crystalline. As shown in Fig. 2c, distinct crystalline peaks due to hexagonal MoS$_2$ (JCPDS 37-1492) and Mo$_2$S$_3$ (JCPDS 40-0972) phases were detected for the laser-sintered film. These data imply that, compared to the conventional heat-sintering method, our laser-sintering method is advantageous in the preparation of
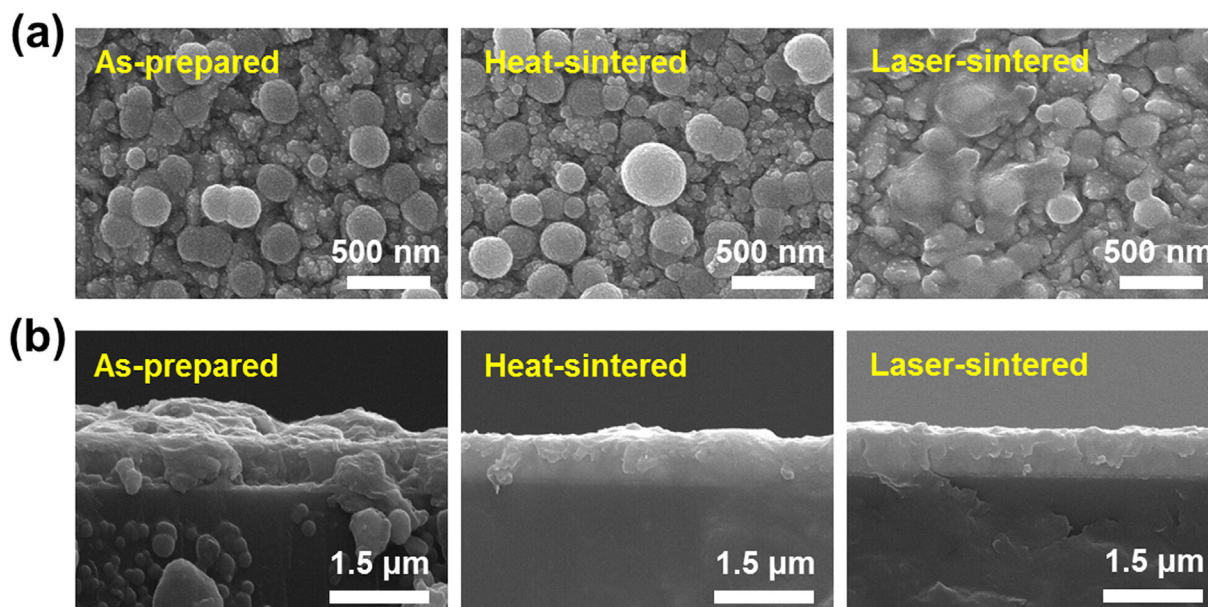

Fig. 1. (a) Surface and (b) cross-sectional SEM images of as-prepared, heat-sintered, and laser-sintered MoS$_2$ films.
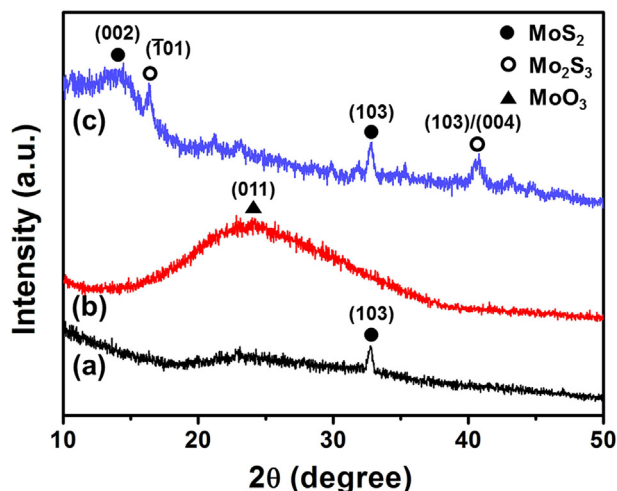
Fig. 2. XRD patterns of (a) as-prepared, (b) heat-sintered, and (c) laser-sintered MoS_2 films.

crystalline molybdenum sulfide films.

XPS measurements were carried out to survey the chemical states of the prepared MoS_2 films before and after the sintering process. Fig. 3 shows the high-resolution Mo 3d and S 2s peaks in XPS spectra for the MoS_2 films. The binding energies (BE) of the Mo(IV) $3d_{5/2}$ and Mo(IV) $3d_{3/2}$ states were 229.5 and 232.7 eV, respectively, for the as-prepared film (Fig. 3a), and these correspond to MoS_2 [36,37]. After heat-sintering (Fig. 3b), peaks due to

Mo(VI) $3d_{5/2}$ (232.4 eV) and Mo(VI) $3d_{3/2}$ (235.6 eV) were detected as well as Mo(IV) $3d_{5/2}$ (228.8 eV) and Mo(IV) $3d_{3/2}$ (231.9 eV) peaks, indicating the presence of MoO_3 [49,50]. This evidence for partial oxidation is in good agreement with the XRD data, as discussed above. On the other hand, for the laser-sintered film, peaks corresponding to Mo(VI) were not detected, as shown in Fig. 3c. As in the case of the as-prepared sample, only Mo(VI) $3d_{5/2}$, Mo(VI) $3d_{3/2}$, and S 2s peaks were detected in the laser-sintered film. The BEs of these peaks were the same as those for the as-prepared sample, and these correspond to MoS_2. However, although the Mo_2S_3 phase was detected in the XRD pattern of the laser-sintered film, XPS peaks corresponding to Mo(III) were not detected.

Because XPS is a surface analysis technique, it is possible that laser-sintering fully sulfurized the Mo species at the film surface. In contrast, the Mo species inside the film were only partially sulfurized, resulting in the observation of the Mo_2S_3 phase. XPS depth profile of the laser-sintered MoS_2 film shown in Fig. S2 (Supplementary Material) also supports this assumption. As the etching time was increased, the atomic ratio between S and Mo was greatly decreased, indicating that the Mo species were not fully sulfurized inside the film.

The electrocatalytic activity of the prepared MoS_2 CEs toward the I^-/I_3^- redox couple before and after sintering was examined by CV analysis, as shown in Fig. 4a. For comparison, a conventional Pt CE was also characterized. Distinct pairs of redox potentials were not observed for the as-prepared CE, and the redox current density was very low, implying inferior electrocatalytic activity for the I^-/I_3^- redox couple. On the other hand, the other CEs clearly generated two pairs of redox waves. The more positive pair relates to the I_2/I_3^- redox reaction, while the more negative pair is related to the I^-/I_3^-
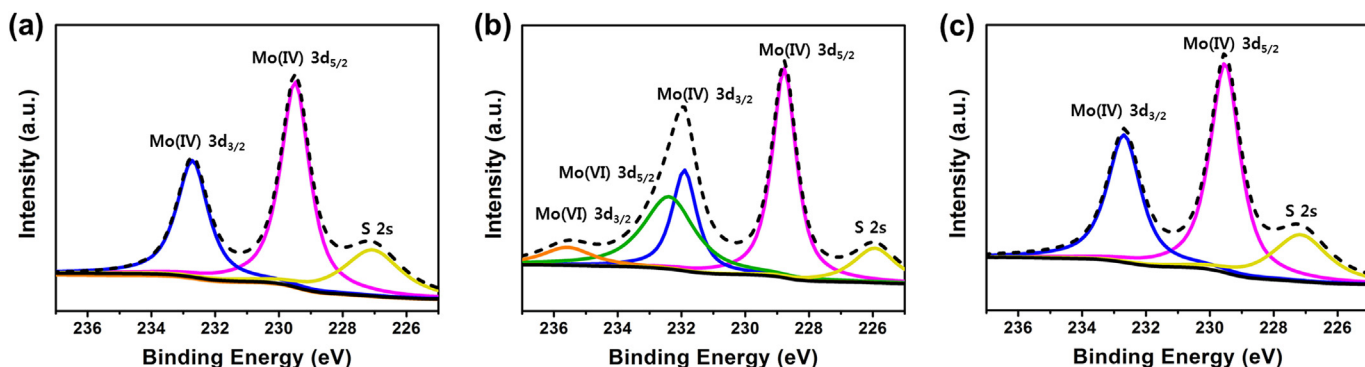

Fig. 3. XPS spectra of (a) as-prepared, (b) heat-sintered, and (c) laser-sintered MoS_2 films.
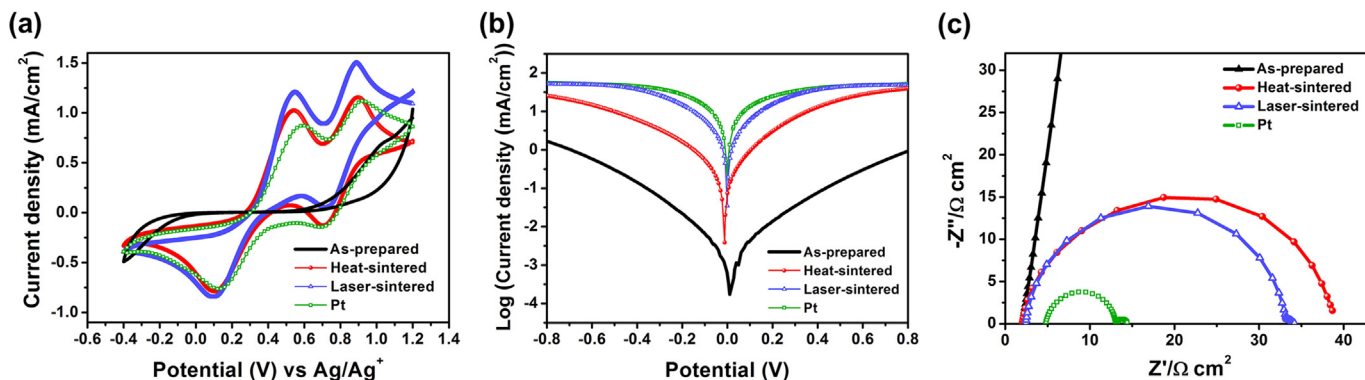

Fig. 4. (a) Cyclic voltammograms of as-prepared, heat-sintered, laser-sintered MoS_2, and Pt CEs for the I^-/I_3^- redox electrolyte. (b) Tafel polarization curves and (c) impedance spectra of symmetric dummy cells with each CE for the I^-/I_3^- redox electrolyte.

redox reaction [25,51]. Both heat- and laser-sintered MoS_2 CEs have comparable redox current densities for the I^-/I_3^- redox reaction to that of the Pt CE. Fig. 4b shows the Tafel polarization curves of symmetric dummy cells with each CE [26,29,52]. The exchange current density (J_0) can be estimated from the intersection of the extrapolated linear anodic and cathodic branches. A steeper slope of the Tafel curve signifies a higher J_0 and greater electrocatalytic activity. As shown in Fig. 4b, the laser-sintered MoS_2 CE exhibited slightly lower J_0 than that of the Pt CE but a much higher J_0 than that of the heat-sintered MoS_2 CE. This result implies that laser-sintering can enhance the electrocatalytic activity of the CE compared to conventional heat-sintering.

To quantitatively compare the electrocatalytic activities of the CEs, we measured the impedance spectra from the same symmetric dummy cells (Fig. 4c). To fit each impedance spectrum, the equivalent circuit model shown in Fig. S3 (Supplementary Material) was used. This equivalent circuit is composed of the series resistance (R_s), the impedance at the electrolyte/CE (R_{ct} and CPE), and the finite Warburg impedance (W_s). W_s is related to electrolyte diffusion, and the constant phase element (CPE) is used for electrodes with rough surfaces instead of a capacitor [51,53]. From the CPE parameters, double-layer capacitance (C_{dl}) can be evaluated. By fitting the impedance spectra using the ZView software, we evaluated R_{ct} and C_{dl}, which are related to electrocatalytic activity, and are listed in Table 1. The R_{ct} of as-prepared CE was reduced by three orders of magnitude after both heat- and laser-sintering. The laser-sintered CE exhibited a lower R_{ct} compared to the heat-sintered CE, indicating superior electrocatalytic activity. Compared to the conventional Pt CE, the laser-sintered CE had a higher R_{ct}; however, it also had a greater value of C_{dl} due to a larger surface area for electrochemical reaction. The results of CV, Tafel polarization measurements, and impedance analysis indicate that the electrocatalytic activity of laser-sintered MoS_2 CE is slightly lower than that of Pt CE but superior to that of the heat-sintered MoS_2 CE. The superior electrocatalytic activity of the laser-sintered CE may be attributed to the enhanced interconnections between the MoS_2

particles and improved crystallinity, as already discussed above.

Finally, each CE was introduced into the DSSCs containing an I^-/I_3^- redox electrolyte, and the photovoltaic performances were compared. The photovoltaic performance parameters obtained from the *J-V* characteristics of the DSSCs with each CE (Fig. 5a) are summarized in Table 1. Both heat- and laser-sintered CEs showed greatly enhanced fill factors (*FF*) and conversion efficiencies compared to the as-prepared CE. These improvements are due to the superior electrocatalytic activity. However, compared to the case of heat-sintered CE ($\eta = 5.96\%$), the conversion efficiency increased by approximately 21% for the laser-sintered CE ($\eta = 7.19\%$). The enhanced photovoltaic performance of laser-sintered CE is attributed to the superior electrocatalytic activity. The conversion efficiency of laser-sintered CE was even comparable with that of the Pt CE ($\eta = 7.42\%$).

Fig. 5b shows IPCE spectra as a function of the incident wavelength of the DSSCs containing each CE. All CEs yielded similar IPCE spectra, which arise from the spectral response of the N-719-containing DSSCs. Despite their similarities, the laser-sintered CE showed an enhanced IPCE in the long-wavelength region (>670 nm), compared to those of the heat-sintered CE and Pt CE. This result indicates that the laser-sintered CE has a superior light scattering effect, resulting in a higher J_{SC}. The validity of solar cell data can be checked by computing the integrated photocurrent from the IPCE spectrum and comparing that with the value of J_{SC} obtained from the *J-V* curves [54,55]. The integrated photocurrents from the IPCE spectra, calculated using publicly available data for AM 1.5 G solar irradiation [56], are 11.79, 12.32, 13.53, and 13.52 mA/cm^2 for the as-prepared, heat-sintered, laser-sintered MoS_2, and Pt CE, respectively. The discrepancies between these values and the values of J_{SC} listed in Table 1 range from 1 to 9%, which is deemed an acceptable range [54,55].

In order to determine whether the heat-sintered MoS_2 CE without oxygen contamination can surpass the performance of laser-sintered CE, we tested the MoS_2 CE prepared with the heat-sintering in a forming gas (5 vol% H_2 in N_2). Fig. S4a

Table 1
Summary of *J-V* characteristics of the DSSCs with as-prepared, heat-sintered, laser-sintered MoS_2, and Pt CEs and parameters determined by fitting the impedance spectra of symmetric dummy cells with each CE.

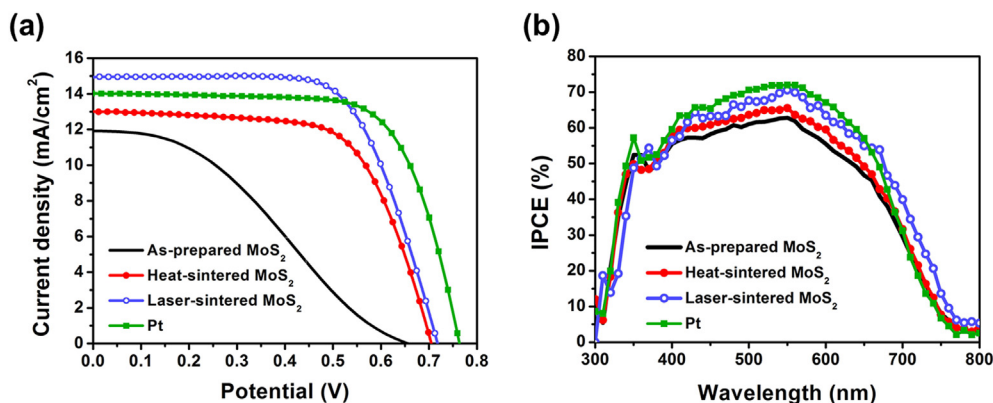| Counter electrode	J_{SC} (mA/cm^2)	V_{OC} (mV)	Fill factor (%)	Efficiency (%)	R_{ct} ($\Omega\ cm^2$)	C_{dl} ($\mu F/cm^2$)
As-prepared	11.92	656	35	2.74	1.01×10^4	33.81
Heat-sintered	13.01	705	65	5.96	18.50	40.97
Laser-sintered	14.94	718	67	7.19	15.29	27.58
Pt	14.30	741	70	7.42	3.99	16.94

Fig. 5. (a) *J-V* characteristics under illumination (light intensity: 100 mW/cm^2, AM 1.5G filter) and (b) IPCE spectra of the DSSCs with as-prepared, heat-sintered, laser-sintered MoS_2, and Pt CEs.

(Supplementary Material) shows XPS spectrum of the MoS_2 film prepared with the heat-sintering in a forming gas. Unlike the case of heat-sintering under a N_2 atmosphere, XPS peaks corresponding to Mo(VI) were not detected, meaning that the MoS_2 film was not oxidized. However, when applied in the DSSC, the photovoltaic performance was inferior to that of the heat-sintered CE under a N_2 atmosphere. As shown in Fig. S4b (Supplementary Material), the conversion efficiency obtained from the *J-V* characteristics was 3.93%, which is much lower compared to the case of heat-sintered CE under a N_2 atmosphere. According to the previous study, the heat-sintering of MoS_2 film in a forming gas at a high temperature (>300 °C) can lead to partial removal of surface sulfur by hydrogenation [57], which may be one of the main reasons for the obtained poor performance as the CE in our study. This result implies that the surface chemical state of MoS_2 film significantly affects to the electrocatalytic activity, and therefore the superior electrocatalytic activity of the laser-sintered MoS_2 CE is closely related with its surface chemical state.

Although the conversion efficiency of 7.19% obtained in this study is lower than the record efficiencies of Pt-free CEs [31-42], it is promising for the DSSCs using MoS_2 CEs. To date, several papers have been reported on DSSCs using the I^-/I_3^- redox electrolyte and MoS_2 CEs, which exhibited high conversion efficiencies of 6.35—8.4% [12—14]. However, the validity of these solar cell data are not guaranteed, either because IPCE measurements were not performed in these studies or the integrated J_{SC} values from the reported IPCE spectra were unreasonably low compared to the value of J_{SC} obtained from the *J-V* curves, as summarized in Table S2 (Supplementary Material). In addition, in those reports, high temperatures (300—800 °C) were required either to prepare MoS_2 or during the post-sintering processes. In contrast, in this work, all processes (the synthesis of MoS_2 at 70 °C and post-sintering at room temperature) were carried out at low temperatures. Furthermore, the post sintering process required only 1 min. Despite this simple and fast process, the prepared MoS_2 CEs was highly efficient, and the IPCE data were reasonable, implying that the laser-sintering process proposed in this study is a promising way to prepare highly efficient MoS_2 CEs.

4. Conclusions

In this study, we developed a simple and rapid fabrication process for efficient MoS_2 electrocatalytic CEs for use in photoelectrochemical DSSCs. Conventional MoS_2 CEs are prepared at high temperatures (200—800 °C) for synthesis and post-sintering; in contrast, using our process, highly efficient MoS_2 CEs were prepared at a low temperature (≤70 °C) *via* a simple process. In particular, instead of the conventional heat-sintering method, the deposited MoS_2 films were post-treated by exposure to a near-infrared (IR) pulsed laser for only 1 min. The laser-sintered MoS_2 films showed enhanced crystallinity and improved interconnections between the MoS_2 particles compared to the heat-sintered MoS_2 films, and these changes led to the superior electrocatalytic activity observed. When used in DSSCs with the I^-/I_3^- redox electrolyte, the laser-sintered MoS_2 CEs exhibited a higher conversion efficiency ($\eta = 7.19\%$) than that of the heat-sintered MoS_2 CEs ($\eta = 5.96\%$) despite the rapid and mild processing laser-sintering conditions. The conversion efficiency was even comparable to that of the conventional Pt CE ($\eta = 7.42\%$). In addition, the fabrication process proposed in this study is compatible with the use of flexible plastic substrates and may offer valuable insights into the development of low-cost photovoltaics.

Appendix A. Supplementary data

Supplementary data related to this article can be found at http://dx.doi.org/10.1016/j.jpowsour.2016.09.002.

References

[1] A.K. Geim, Science 324 (2009) 1530—1534.
[2] M. Chhowalla, H.S. Shin, G. Eda, L.J. Li, K.P. Loh, H. Zhang, Nat. Chem. 5 (2013) 263—275.
[3] S.Z. Butler, S.M. Hollen, L. Cao, Y. Cui, J.A. Gupta, H.R. Gutiérrez, T.F. Heinz, S.S. Hong, J. Huang, A.F. Ismach, E. Johnston-Halperin, M. Kuno, V.V. Plashnitsa, R.D. Robinson, R.S. Ruoff, S. Salahuddin, J. Shan, L. Shi, M.G. Spencer, M. Terrones, W. Windl, J.E. Goldberger, ACS Nano 7 (2013) 2898—2926.
[4] H.-J. Chuang, B. Chamlagain, M. Koehler, M.M. Perera, J. Yan, D. Mandrus, D. Tománek, Z. Zhou, Nano Lett. 16 (2016) 1896—1902.
[5] L. Yu, Y.-H. Lee, X. Ling, E.J.G. Santos, Y.C. Shin, Y. Lin, M. Dubey, E. Kaxiras, J. Kong, H. Wang, T. Palacios, Nano Lett. 14 (2014) 3055—3063.
[6] J.-S. Kim, H.-W. Yoo, H.O. Choi, H.-T. Jung, Nano Lett. 14 (2014) 5941—5947.
[7] X. Cao, Y. Shi, W. Shi, X. Rui, Q. Yan, J. Kong, H. Zhang, Small 9 (2013) 3433—3438.
[8] S.-K. Park, S.-H. Yu, S. Woo, B. Quan, D.-C. Lee, M.K. Kim, Y.-E. Sung, Y. Piao, Dalton Trans. 42 (2013) 2399—2405.
[9] F. Li, J. Li, X. Lin, X. Li, Y. Fang, L. Jiao, X. An, Y. Fu, J. Jin, R. Li, J. Power Sources 300 (2015) 301—308.
[10] N. Liu, L. Yang, S. Wang, Z. Zhong, S. He, X. Yang, Q. Gao, Y. Tang, J. Power Sources 275 (2015) 588—594.
[11] M.-L. Tsai, S.-H. Su, J.-K. Chang, D.-S. Tsai, C.-H. Chen, C.-I. Wu, L.-J. Li, L.-J. Chen, J.-H. He, ACS Nano 8 (2014) 8317—8322.
[12] M. Wu, Y. Wang, X. Lin, N. Yu, L. Wang, L. Wang, A. Hagfeldt, T. Ma, Phys. Chem. Chem. Phys. 13 (2011) 19298—19301.
[13] S.A. Patil, P.Y. Kalode, R.S. Mane, D.V. Shinde, A. Doyoung, C. Keumnam, M.M. Sung, S.B. Ambede, S.-H. Hwan, Dalton Trans. 43 (2014) 5256—5259.
[14] C.-H. Lin, C.-H. Tsai, F.-G. Tseng, Y.-Y. Yu, H.-C. Wu, C.-K. Hsieh, Nanoscale Res. Lett. 10 (2015) 446.
[15] A. Anteonelou, G. Syrrokostas, L. Sygellou, G. Leftheriotis, V. Dracopoulos, S.N. Yannopoulos, Nanotechnology 27 (2015) 045404.
[16] B. Lei, G.R. Li, X.P. Gao, J. Mater. Chem. A 2 (2014) 3919—3925.
[17] J. Zhang, S. Najmaei, H. Lin, J. Lou, Nanoscale 6 (2014) 5279—5283.
[18] M. Zheng, J. Huo, Y. Tu, J. Wu, L. Hu, S. Dai, Electrochim. Acta 173 (2015) 252—259.
[19] B. O'Regan, M. Grätzel, Nature 353 (1991) 737—740.
[20] S. Ito, S.M. Zakeeruddin, P. Comte, P. Liska, D. Kuang, M. Grätzel, Nat. Phot. 2 (2008) 693—698.
[21] A. Hagfeldt, G. Boschloo, L. Sun, L. Kloo, H. Pettersson, Chem. Rev. 110 (2010) 6595—6663.
[22] J.-Y. Kim, S.H. Kang, H.S. Kim, Y.-E. Sung, Langmuir 26 (2010) 2864—2870.
[23] J.-Y. Kim, J.S. Kang, J. Shin, J. Kim, S.-J. Han, J. Park, Y.-S. Min, M.J. Ko, Y.-E. Sung, Nanoscale 7 (2015) 8368—8377.
[24] J.-Y. Kim, K.-H. Lee, J. Shin, S.H. Park, J.S. Kang, K.S. Han, M.M. Sung, N. Pinna, Y.-E. Sung, Nanotechnology 25 (2014) 504003.
[25] K. Yoo, J.-Y. Kim, J.A. Lee, J.S. Kim, D.-K. Lee, K. Kim, J.Y. Kim, B. Kim, H. Kim, W.M. Kim, J.H. Kim, M.J. Ko, ACS Nano 9 (2015) 3760—3771.
[26] J.S. Kang, M.-A. Park, J.-Y. Kim, S.H. Park, D.Y. Chung, S.-H. Yu, J. Kim, J. Park, J.-W. Choi, K.J. Lee, J. Jeong, M.J. Ko, K.-S. Ahn, Y.-E. Sung, Sci. Rep. 5 (2015) 10450.
[27] I. Jeong, J. Lee, K.L.V. Joseph, H.I. Lee, J.K. Kim, S. Yoon, J. Lee, Nano Energy 9 (2014) 392—400.
[28] I. Jeong, C. Jo, A. Anthonysamy, J.-M. Kim, E. Kang, J. Hwang, E. Ramasamy, S.-W. Rhee, J.K. Kim, K.-S. Ha, K.-W. Jun, J. Lee, Chem. Sus. Chem. 6 (2013) 299—307.
[29] M. Wu, X. Lin, Y. Wang, L. Wang, W. Guo, D. Qi, X. Peng, A. Hagfeldt, M. Grätzel, T. Ma, J. Am. Chem. Soc. 134 (2012) 3419—3428.
[30] Y.-C. Wang, D.-Y. Wang, Y.-T. Jiang, H.-A. Chen, C.-C. Chen, K.-C. Ho, H.-L. Chou, C.-W. Chen, Angew. Chem. Int. Ed. 52 (2013) 6694—6698.
[31] Z. Li, F. Gong, G. Zhou, Z.-S. Wang, J. Phys. Chem. C 117 (2013) 6561—6566.
[32] M. Wu, X. Lin, A. Hagfeldt, T. Ma, Angew. Chem. Int. Ed. 50 (2011) 3520—3524.
[33] Q.W. Jiang, G.R. Li, X.P. Gao, Chem. Commun. (2009) 6720—6722.

[34] Q.W. Jiang, G.R. Li, S. Liu, X.P. Gao, J. Phys. Chem. C 114 (2010) 13397—13401.
[35] X. Chen, Q. Tang, B. He, L. Lin, L. Yu, Angew. Chem. Int. Ed. 126 (2014) 10975—10979.
[36] J. Liu, Q. Tang, B. He, L. Yu, J. Power Sources 282 (2015) 79—86.
[37] Y. Duan, Q. Tang, B. He, Z. Zhao, L. Zhu, L. Yu, J. Power Sources 284 (2015) 349—354.
[38] H. Cai, Q. Tang, B. He, R. Li, L. Yu, Nanoscale 6 (2015) 15127—15133.
[39] N. Jeon, D.K. Hwang, Y.S. Kang, S.S. Im, D.-W. Kim, Electrochem. Commun. 34 (2013) 1—4.
[40] H.N. Tsao, J. Burschka, C. Yi, F. Kessler, M.K. Nazeeruddin, M. Grätzel, Energy Environ. Sci. 4 (2011) 4921—4924.
[41] T.N. Murakami, M. Grätzel, Inorg. Chim. Acta 361 (2008) 572—580.
[42] L. Kavan, J.-H. Yum, M.K. Nazeeruddin, M. Grätzel, ACS Nano 5 (2011) 9171—9178.
[43] Y. Li, D.-K. Lee, J.Y. Kim, B. Kim, N.-G. Park, K. Kim, J.-H. Shin, I.-S. Choi, M.J. Ko, Energy Environ. Sci. 5 (2012) 8950—8957.
[44] A. Fakharuddin, R. Jose, T.M. Brown, F. Fabregat-Santiago, J. Bisquert, Energy Environ. Sci. 7 (2014) 3952—3981.
[45] H.J. Koo, J. Park, B. Yoo, K. Yoo, K. Kim, N.-G. Park, Inorg. Chim. Acta 361 (2008) 677—683.
[46] S. Ito, M.K. Nazeeruddin, P. Liska, P. Comte, R. Charvet, P. Péchy, M. Jirousek, A. Kay, S.M. Zakeeruddin, M. Grätzel, Prog. Photovolt. Res. Appl. 14 (2006)

[47] J. Park, H.-J. Koo, B. Yoo, K. Yoo, K. Kim, W. Choi, N.-G. Park, Sol. Energ. Mat. Sol. Cells 91 (2007) 1749—1754.
[48] L. Ratke, P.W. Voorhees, Growth and Coarsening: Ostwald Ripening in Material Processing First ed, Springer, Berlin, 2002.
[49] D. Ganta, S. Sinha, R.T. Haasch, Surf. Sci. Spectra 21 (2014) 19—27.
[50] M.A. Baker, R. Gilmore, C. Lenardi, W. Gissler, Appl. Surf. Sci. 150 (1999) 255—262.
[51] J.D. Roy-Mayhew, D.J. Bozym, C. Punckt, I.A. Aksay, ACS Nano 4 (2010) 6203—6211.
[52] J.-Y. Kim, J.Y. Lee, K.-Y. Shin, H. Jeong, H.J. Son, C.-H. Lee, J.H. Park, S.-S Lee, J.G. Son, M.J. Ko, Appl. Catal. B Environ. 192 (2016) 342—349.
[53] J.-Y. Kim, K.J. Lee, S.H. Kang, J. Shin, Y.-E. Sung, J. Phys. Chem. C 115 (2011) 19979—19985.
[54] E. Zimmermann, P. Ehrenreich, T. Pfadler, J.A. Dorman, J. Weickert, L. Schmidt-Mende, Nat. Photonics 8 (2014) 669—672.
[55] J.A. Christians, J.S. Manser, P.V. Kamat, J. Phys. Chem. Lett. 6 (2015) 852—857.
[56] ASTM G173—03, Standard Tables for Reference Solar Spectral Irradiances: Direct Normal and Hemispherical on 37° Tilted Surface, American Society for Testing and Materials, West Conshohocken, PA, 2012.
[57] X.S. Li, Q. Xin, X.X. Guo, P. Grange, B. Delmon, J. Catal. 137 (1992) 385—393.

589—601.